Multiparameter entanglement in quantum interferometry

Mete Atatüre,[1] Giovanni Di Giuseppe,[2] Matthew D. Shaw,[2] Alexander V. Sergienko,[1,2] Bahaa E. A. Saleh,[2] and Malvin C. Teich[1,2]

[1]*Quantum Imaging Laboratory, Department of Physics, Boston University, 8 Saint Mary's Street, Boston, Massachusetts 02215*

[2]*Quantum Imaging Laboratory, Department of Electrical and Computer Engineering, Boston University, 8 Saint Mary's Street, Boston, Massachusetts 02215*

(Received 28 June 2001; revised manuscript received 26 October 2001; published 30 August 2002)

The role of multiparameter entanglement in quantum interference from collinear Type-II spontaneous parametric down-conversion is explored using a variety of aperture shapes and sizes, in regimes of both ultrafast and continuous-wave pumping. We have developed and experimentally verified a theory of down-conversion which considers a quantum state that can be concurrently entangled in frequency, wavevector, and polarization. In particular, we demonstrate deviations from the familiar triangular interference dip, such as asymmetry and peaking. These findings improve our capacity to control the quantum state produced by spontaneous parametric down-conversion, and should prove useful to those pursuing the many proposed applications of down-converted light.

DOI: 10.1103/PhysRevA.66.023822 PACS number(s): 42.50.Dv, 42.65.Re, 42.65.Ky, 03.67.−a

I. INTRODUCTION

In the nonlinear-optical process of spontaneous parametric down-conversion (SPDC) [1], in which a laser beam illuminates a nonlinear-optical crystal, pairs of photons are generated in a state that can be entangled [2] concurrently in frequency, momentum, and polarization. A significant number of experimental efforts designed to verify the entangled nature of such states have been carried out on states entangled in a *single* parameter, such as in energy [3], momentum [4], or polarization [5]. In general, the quantum state produced by SPDC is not factorizable into independently entangled single-parameter functions. Consequently any attempt to access one parameter is affected by the presence of the others. A common approach to quantum interferometry to date has been to choose a single entangled parameter of interest and eliminate the dependence of the quantum state on all other parameters. For example, when investigating polarization entanglement, spectral and spatial filtering are typically imposed in an attempt to restrict attention to polarization alone.

A more general approach to this problem is to consider and exploit the concurrent entanglement from the outset. In this approach, the observed quantum-interference pattern in one parameter, such as polarization, can be modified at will by controlling the dependence of the state on the other parameters, such as frequency and transverse wave vector. This strong interdependence has its origin in the nonfactorizability of the quantum state into product functions of the separate parameters.

In this paper we theoretically and experimentally study how the polarization quantum-interference pattern, presented as a function of relative temporal delay between the photons of an entangled pair, is modified by controlling the optical system through different kinds of spatial apertures. The effect of the spectral profile of the pump field is investigated by using both a continuous wave and a pulsed laser to generate SPDC. The role of the spatial profile of the pump field is also studied experimentally by restricting the pump-beam diameter at the face of the nonlinear crystal.

Spatial effects in Type-I SPDC have previously been investigated, typically in the context of imaging with spatially resolving detection systems [6]. The theoretical formalism presented here for Type-II SPDC is suitable for extension to Type-I in the presence of an arbitrary optical system and detection apparatus. Our study leads to a deeper physical understanding of multiparameter entangled two-photon states and concomitantly provides a route for engineering these states for specific applications, including quantum information processing.

II. MULTIPARAMETER ENTANGLED-STATE FORMALISM

In this section we present a multidimensional analysis of the entangled-photon state generated via Type-II SPDC. To admit a broad range of possible experimental schemes we consider, in turn, the three distinct stages of any experimental apparatus: the generation, propagation, and detection of the quantum state [7].

A. Generation

By virtue of the relatively weak interaction in the nonlinear crystal, we consider the two-photon state generated within the confines of first-order time-dependent perturbation theory,

$$|\Psi^{(2)}\rangle \sim \frac{\mathrm{i}}{\hbar}\int_{t_0}^{t} dt' \hat{H}_{\mathrm{int}}(t')|0\rangle. \tag{1}$$

Here $\hat{H}_{\mathrm{int}}(t')$ is the interaction Hamiltonian, $[t_0,t]$ is the duration of the interaction, and $|0\rangle$ is the initial vacuum state. The interaction Hamiltonian governing this phenomenon is [8]

$$\hat{H}_{\mathrm{int}}(t') \sim \chi^{(2)} \int_V d\mathbf{r}\, \hat{E}_p^{(+)}(\mathbf{r},t')\hat{E}_o^{(-)}(\mathbf{r},t')\hat{E}_e^{(-)}(\mathbf{r},t') + \mathrm{H.c.}, \tag{2}$$

where $\chi^{(2)}$ is the second-order susceptibility and V is the volume of the nonlinear medium in which the interaction takes place. The operator $\hat{E}_j^{(\pm)}(\mathbf{r},t')$ represents the positive-(negative-) frequency portion of the jth electric-field operator, with the subscript j representing the pump (p), ordinary (o), and extraordinary (e) waves at position $\mathbf{r}$ and time t', and H.c. stands for Hermitian conjugate. Due to the high intensity of the pump field it can be represented by a classical c-number, rather than as an operator, with an arbitrary spatiotemporal profile given by

$$E_p(\mathbf{r},t)=\int d\mathbf{k}_p\,\tilde{E}_p(\mathbf{k}_p)e^{i\mathbf{k}_p\cdot\mathbf{r}}e^{-i\omega_p(\mathbf{k}_p)t}, \tag{3}$$

where $\tilde{E}_p(\mathbf{k}_p)$ is the complex-amplitude profile of the field as a function of the wave vector $\mathbf{k}_p$.

We decompose the three-dimensional wave vector $\mathbf{k}_p$ into a two-dimensional transverse wave vector $\mathbf{q}_p$ and frequency ω_p, so that Eq. (3) takes the form

$$E_p(\mathbf{r},t)=\int d\mathbf{q}_p\,d\omega_p\,\tilde{E}_p(\mathbf{q}_p;\omega_p)e^{i\kappa_p z}e^{i\mathbf{q}_p\cdot\mathbf{x}}e^{-i\omega_p t}, \tag{4}$$

where $\mathbf{x}$ spans the transverse plane perpendicular to the propagation direction z. In a similar way the ordinary and extraordinary fields can be expressed in terms of the quantum-mechanical creation operators $\hat{a}^\dagger(\mathbf{q},\omega)$ for the $(\mathbf{q},\omega)$ modes as

$$\hat{E}_j^{(-)}(\mathbf{r},t)=\int d\mathbf{q}_j\,d\omega_j\,e^{-i\kappa_j z}e^{-i\mathbf{q}_j\cdot\mathbf{x}}e^{i\omega_j t}\,\hat{a}_j^\dagger(\mathbf{q}_j,\omega_j), \tag{5}$$

where the subscript $j=o,e$. The longitudinal component of $\mathbf{k}$, denoted κ, can be written in terms of the $(\mathbf{q},\omega)$ pair as [7,9]

$$\kappa=\sqrt{\left[\frac{n(\omega,\theta)\omega}{c}\right]^2-|\mathbf{q}|^2}, \tag{6}$$

where c is the speed of light in vacuum, θ is the angle between $\mathbf{k}$ and the optical axis of the nonlinear crystal (see Fig. 1), and $n(\omega,\theta)$ is the index of refraction in the nonlinear medium. Note that the symbol $n(\omega,\theta)$ in Eq. (6) represents the extraordinary refractive index $n_e(\omega,\theta)$ when calculating κ for extraordinary waves, and the ordinary refractive index $n_o(\omega)$ for ordinary waves.

Substituting Eqs. (4) and (5) into Eqs. (1) and (2) yields the quantum state at the output of the nonlinear crystal,

$$|\Psi^{(2)}\rangle\sim\int d\mathbf{q}_o d\mathbf{q}_e\,d\omega_o d\omega_e\,\Phi(\mathbf{q}_o,\mathbf{q}_e;\omega_o,\omega_e)\times\hat{a}_o^\dagger(\mathbf{q}_o,\omega_o)\hat{a}_e^\dagger(\mathbf{q}_e,\omega_e)|0\rangle, \tag{7}$$

with

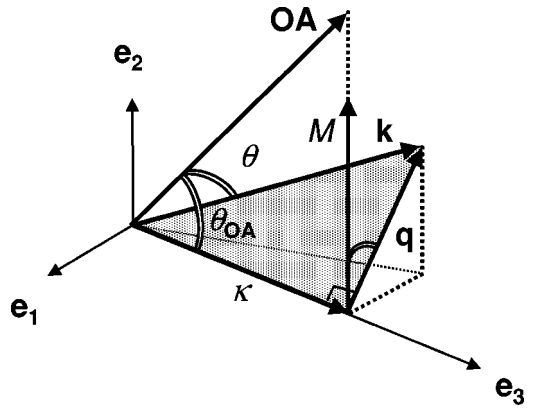

FIG. 1. Decomposition of a three-dimensional wave vector $(\mathbf{k})$ into longitudinal (κ) and transverse $(\mathbf{q})$ components. The angle between the optical axis (OA) of the nonlinear crystal and the wave vector $\mathbf{k}$ is θ. The angle between the optical axis and the longitudinal axis $(\mathbf{e}_3)$ is denoted θ_{OA}. The spatial walk-off of the extraordinary polarization component of a field traveling through the nonlinear crystal is characterized by the quantity M.

$$\Phi(\mathbf{q}_o,\mathbf{q}_e;\omega_o,\omega_e)=\tilde{E}_p(\mathbf{q}_o+\mathbf{q}_e;\omega_o+\omega_e)\times L\,\mathrm{sinc}\left(\frac{L\Delta}{2}\right)e^{-iL\Delta/2}, \tag{8}$$

where L is the thickness of the crystal and $\Delta=\kappa_p-\kappa_o-\kappa_e$ where κ_j $(j=p,o,e)$ is related to the indices $(\mathbf{q}_j,\omega_j)$ via relations similar to Eq. (6). The nonseparability of the function $\Phi(\mathbf{q}_o,\mathbf{q}_e;\omega_o,\omega_e)$ in Eqs. (7) and (8), recalling Eq. (6), is the hallmark of *concurrent* multiparameter entanglement.

B. Propagation

Propagation of the down-converted light between the planes of generation and detection is characterized by the transfer function of the optical system. The biphoton probability amplitude [8] at the space-time coordinates $(\mathbf{x}_A,t_A)$ and $(\mathbf{x}_B,t_B)$ where detection takes place is defined by

$$A(\mathbf{x}_A,\mathbf{x}_B;t_A,t_B)=\langle 0|\hat{E}_A^{(+)}(\mathbf{x}_A,t_A)\hat{E}_B^{(+)}(\mathbf{x}_B,t_B)|\Psi^{(2)}\rangle. \tag{9}$$

The explicit forms of the quantum operators at the detection locations are represented by [7]

$$\hat{E}_A^{(+)}(\mathbf{x}_A,t_A)=\int d\mathbf{q}\,d\omega\,e^{-i\omega t_A}[\mathcal{H}_{Ae}(\mathbf{x}_A,\mathbf{q};\omega)\hat{a}_e(\mathbf{q},\omega)+\mathcal{H}_{Ao}(\mathbf{x}_A,\mathbf{q};\omega)\hat{a}_o(\mathbf{q},\omega)],$$

$$\hat{E}_B^{(+)}(\mathbf{x}_B,t_B)=\int d\mathbf{q}\,d\omega\,e^{-i\omega t_B}[\mathcal{H}_{Be}(\mathbf{x}_B,\mathbf{q};\omega)\hat{a}_e(\mathbf{q},\omega)+\mathcal{H}_{Bo}(\mathbf{x}_B,\mathbf{q};\omega)\hat{a}_o(\mathbf{q},\omega)], \tag{10}$$

where the transfer function $\mathcal{H}_{ij}$ $(i=A,B$ and $j=e,o)$ describes the propagation of a $(\mathbf{q},\omega)$ mode from the nonlinear-

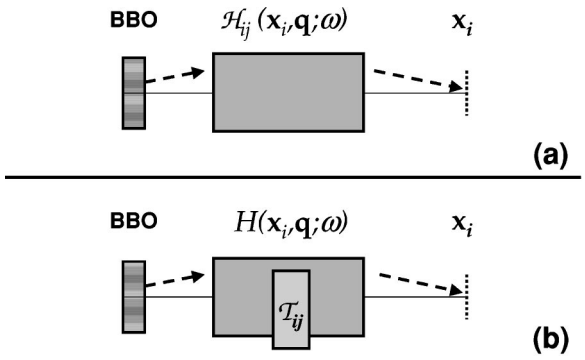

FIG. 2. (a) Illustration of the idealized setup for observation of quantum interference using SPDC. BBO represents a beta-barium borate nonlinear optical crystal, $\mathcal{H}_{ij}(\mathbf{x}_i,\mathbf{q};\omega)$ is the transfer function of the system, and the detection plane is represented by $\mathbf{x}_i$. (b) For most experimental configurations the transfer function can be factorized into diffraction-dependent $[H(\mathbf{x}_i,\mathbf{q};\omega)]$ and diffraction-independent $(\mathcal{T}_{ij})$ components.

crystal output plane to the detection plane. Substituting Eqs. (7) and (10) into Eq. (9) yields a general form for the biphoton probability amplitude,

$$A(\mathbf{x}_A,\mathbf{x}_B;t_A,t_B)=\int d\mathbf{q}_o d\mathbf{q}_e\, d\omega_o d\omega_e\, \Phi(\mathbf{q}_o,\mathbf{q}_e;\omega_o,\omega_e) \times[\mathcal{H}_{Ae}(\mathbf{x}_A,\mathbf{q}_e;\omega_e)\mathcal{H}_{Bo}(\mathbf{x}_B,\mathbf{q}_o;\omega_o) \times e^{-\mathrm{i}(\omega_e t_A+\omega_o t_B)}+\mathcal{H}_{Ao}(\mathbf{x}_A,\mathbf{q}_o;\omega_o) \times\mathcal{H}_{Be}(\mathbf{x}_B,\mathbf{q}_e;\omega_e)\, e^{-\mathrm{i}(\omega_o t_A+\omega_e t_B)}]. \quad (11)$$

By choosing optical systems with explicit forms of the functions $\mathcal{H}_{Ae}$, $\mathcal{H}_{Ao}$, $\mathcal{H}_{Be}$, and $\mathcal{H}_{Bo}$, the overall biphoton probability amplitude can be constructed as desired.

C. Detection

The formulation of the detection process requires some knowledge of the detection apparatus. Slow detectors, for example, impart temporal integration while detectors of finite area impart spatial integration. One extreme case is realized when the temporal response of a *point* detector is spread negligibly with respect to the characteristic time scale of SPDC, namely, the inverse of down-conversion bandwidth. In this limit the coincidence rate reduces to

$$R=|A(\mathbf{x}_A,\mathbf{x}_B;t_A,t_B)|^2. \quad (12)$$

On the other hand, quantum-interference experiments typically make use of slow *bucket* detectors. Under these conditions, the coincidence count rate R is readily expressed in terms of the biphoton probability amplitude as

$$R=\int d\mathbf{x}_A d\mathbf{x}_B\, dt_A dt_B\, |A(\mathbf{x}_A,\mathbf{x}_B;t_A,t_B)|^2. \quad (13)$$

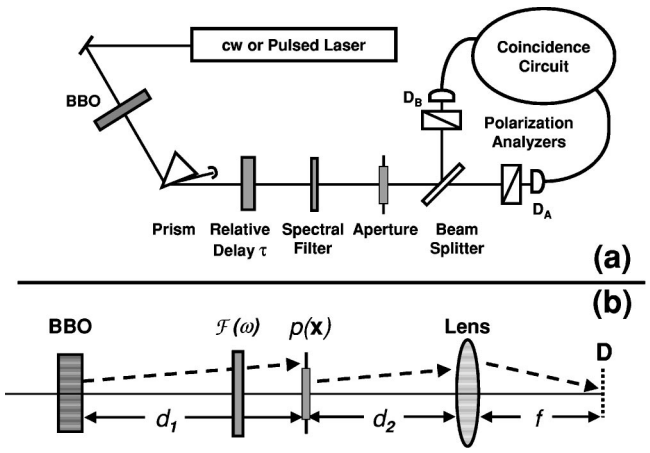

FIG. 3. (a) Schematic of the experimental setup for observation of quantum interference using Type-II collinear SPDC (see text for details). (b) Detail of the path from the crystal output plane to the detector input plane. $\mathcal{F}(\omega)$ represents an (optional) filter transmission function, $p(\mathbf{x})$ represents an aperture function, and f is the focal length of the lens.

III. MULTIPARAMETER ENTANGLED-STATE MANIPULATION

In this section we apply the mathematical description presented above to specific configurations of a quantum interferometer. Since the evolution of the state is ultimately described by the transfer function $\mathcal{H}_{ij}$, an explicit form of this function is needed for each configuration of interest. Almost all quantum-interference experiments performed to date have a common feature, namely, that the transfer function $\mathcal{H}_{ij}$ in Eq. (11), with $i=A,B$ and $j=o,e$, can be separated into diffraction-dependent and -independent terms as

$$\mathcal{H}_{ij}(\mathbf{x}_i,\mathbf{q};\omega)=\mathcal{T}_{ij}\,H(\mathbf{x}_i,\mathbf{q};\omega), \quad (14)$$

where the diffraction-dependent terms are grouped in H and the diffraction-independent terms are grouped in $\mathcal{T}_{ij}$ (see Fig. 2). Free space, apertures, and lenses, for example, can be treated as diffraction-dependent elements while beam splitters, temporal delays, and wave plates can be considered as diffraction-independent elements. For collinear SPDC configurations, for example, in the presence of a relative optical-path delay τ between the ordinary and the extraordinary polarized photons, as illustrated in Fig. 3(a), $\mathcal{T}_{ij}$ is simply

$$\mathcal{T}_{ij}=(\mathbf{e}_i\cdot\mathbf{e}_j)\, e^{-\mathrm{i}\omega\tau\delta_{ej}}, \quad (15)$$

where the symbol δ_{ej} is the Kronecker delta with $\delta_{ee}=1$ and $\delta_{eo}=0$. The unit vector $\mathbf{e}_i$ describes the orientation of each polarization analyzer in the experimental apparatus, while $\mathbf{e}_j$ is the unit vector that describes the polarization of each down-converted photon.

Using the expression for $\mathcal{H}_{ij}$ given in Eq. (14) in the general biphoton probability amplitude given in Eq. (11), we construct a compact expression for all systems that can be separated into diffraction-dependent and -independent elements as

$$A(\mathbf{x}_A,\mathbf{x}_B;t_A,t_B)=\int d\mathbf{q}_o d\mathbf{q}_e\, d\omega_o d\omega_e\, \Phi(\mathbf{q}_o,\mathbf{q}_e;\omega_o,\omega_e)$$
$$\times[\mathcal{T}_{Ae}H(\mathbf{x}_A,\mathbf{q}_e;\omega_e)\mathcal{T}_{Bo}H(\mathbf{x}_B,\mathbf{q}_o;\omega_o)$$
$$\times e^{-\mathrm{i}(\omega_e t_A+\omega_o t_B)}+\mathcal{T}_{Ao}H(\mathbf{x}_A,\mathbf{q}_o;\omega_o)$$
$$\times\mathcal{T}_{Be}H(\mathbf{x}_B,\mathbf{q}_e;\omega_e)\, e^{-\mathrm{i}(\omega_o t_A+\omega_e t_B)}]. \tag{16}$$

Given the general form of the biphoton probability amplitude for a separable system, we now proceed to investigate several specific experimental arrangements. For the experimental work presented in this paper the angle between $\mathbf{e}_i$ and $\mathbf{e}_j$ is 45°, so $\mathcal{T}_{ij}$ can be simplified by using $(\mathbf{e}_i\cdot\mathbf{e}_j)=\pm 1/\sqrt{2}$ [5]. Substituting this into Eq. (16), the biphoton probability amplitude becomes

$$A(\mathbf{x}_A,\mathbf{x}_B;t_A,t_B)=\int d\mathbf{q}_o d\mathbf{q}_e\, d\omega_o d\omega_e\, \tilde{E}_p(\mathbf{q}_o+\mathbf{q}_e;\omega_o+\omega_e)$$
$$\times L\,\mathrm{sinc}\left(\frac{L\Delta}{2}\right)e^{-\mathrm{i}L\Delta/2}\,e^{-\mathrm{i}\omega_e\tau}$$
$$\times[H(\mathbf{x}_A,\mathbf{q}_e;\omega_e)H(\mathbf{x}_B,\mathbf{q}_o;\omega_o)$$
$$\times e^{-\mathrm{i}(\omega_e t_A+\omega_o t_B)}-H(\mathbf{x}_A,\mathbf{q}_o;\omega_o)H(\mathbf{x}_B,\mathbf{q}_e;\omega_e)$$
$$\times e^{-\mathrm{i}(\omega_o t_A+\omega_e t_B)}] \tag{17}$$

where $\mathrm{sinc}(x)\equiv\sin(x)/x$. Substitution of Eq. (17) into Eq. (13) gives an expression for the coincidence-count rate given an arbitrary pump profile and optical system.

However, this expression is unwieldy for purposes of predicting interference patterns except in certain cases, where integration can be swiftly performed. In particular, we consider three cases of the spatial and spectral profiles of the pump field in Eq. (17): (1) a polychromatic plane wave, (2) a monochromatic plane wave, and (3) a monochromatic beam with arbitrary spatial profile. These various cases will be used subsequently for cw and pulse-pumped SPDC studies.

First, a nonmonochromatic plane-wave pump field is described mathematically by

$$\tilde{E}_p(\mathbf{q}_p;\omega_p)=\delta(\mathbf{q}_p)\mathcal{E}_p(\omega_p-\omega_p^0), \tag{18}$$

where $\mathcal{E}_p(\omega_p-\omega_p^0)$ is the spectral profile of the pump field. Equation (17) then takes the form

$$A(\mathbf{x}_A,\mathbf{x}_B;t_A,t_B)=\int d\mathbf{q}\, d\omega_o d\omega_e\, \mathcal{E}_p(\omega_o+\omega_e-\omega_p^0)$$
$$\times L\,\mathrm{sinc}\left(\frac{L\Delta}{2}\right)e^{-\mathrm{i}L\Delta/2}\,e^{-\mathrm{i}\omega_e\tau}$$
$$\times[H(\mathbf{x}_A,\mathbf{q};\omega_e)H(\mathbf{x}_B,-\mathbf{q};\omega_o)$$
$$\times e^{-\mathrm{i}(\omega_e t_A+\omega_o t_B)}-H(\mathbf{x}_A,-\mathbf{q};\omega_o)$$
$$\times H(\mathbf{x}_B,\mathbf{q};\omega_e)\, e^{-\mathrm{i}(\omega_o t_A+\omega_e t_B)}]. \tag{19}$$

Second, a monochromatic plane-wave pump field is described by

$$\tilde{E}_p(\mathbf{q}_p;\omega_p)=\delta(\mathbf{q}_p)\,\delta(\omega_p-\omega_p^0), \tag{20}$$

whereupon Eq. (19) becomes

$$A(\mathbf{x}_A,\mathbf{x}_B;t_A,t_B)=\int d\mathbf{q}\, d\omega\, L\,\mathrm{sinc}\left(\frac{L\Delta}{2}\right)$$
$$\times e^{-\mathrm{i}L\Delta/2}\,e^{-\mathrm{i}\omega\tau}\,e^{-\mathrm{i}\omega_p^0(t_A+t_B)}[H(\mathbf{x}_A,\mathbf{q};\omega)$$
$$\times H(\mathbf{x}_B,-\mathbf{q};\omega_p^0-\omega)\, e^{-\mathrm{i}\omega(t_A-t_B)}$$
$$-H(\mathbf{x}_A,-\mathbf{q};\omega_p^0-\omega)H(\mathbf{x}_B,\mathbf{q};\omega)$$
$$\times e^{\mathrm{i}\omega(t_A-t_B)}]. \tag{21}$$

In this case the nonfactorizability of the state is due solely to the phase matching.

Third, we examine the effect of the spatial distribution of the pump field by considering a monochromatic field with an arbitrary spatial profile described by

$$\tilde{E}_p(\mathbf{q}_p;\omega_p)=\Gamma(\mathbf{q}_p)\,\delta(\omega_p-\omega_p^0), \tag{22}$$

where $\Gamma(\mathbf{q}_p)$ characterizes the spatial profile of the pump field through transverse wave vectors. In this case Eq. (17) simplifies to

$$A(\mathbf{x}_A,\mathbf{x}_B;t_A,t_B)=\int d\mathbf{q}_o d\mathbf{q}_e\, d\omega\,\Gamma(\mathbf{q}_e+\mathbf{q}_o)\, L\,\mathrm{sinc}\left(\frac{L\Delta}{2}\right)$$
$$\times e^{-\mathrm{i}L\Delta/2}\,e^{-\mathrm{i}\omega\tau}\,e^{-\mathrm{i}\omega_p^0(t_A+t_B)}$$
$$\times[H(\mathbf{x}_A,\mathbf{q}_e;\omega)H(\mathbf{x}_B,\mathbf{q}_o;\omega_p^0-\omega)$$
$$\times e^{-\mathrm{i}\omega(t_A-t_B)}-H(\mathbf{x}_A,\mathbf{q}_o;\omega_p^0-\omega)$$
$$\times H(\mathbf{x}_B,\mathbf{q}_e;\omega)\, e^{\mathrm{i}\omega(t_A-t_B)}]. \tag{23}$$

Using Eq. (21) as the biphoton probability amplitude for cw-pumped SPDC and Eq. (19) for pulse-pumped SPDC in Eq. (13), we can now investigate the behavior of the quantum-interference pattern for optical systems described by specific transfer functions H. Equation (23) will be considered in Sec. III C to investigate the limit where the pump spatial profile has a considerable effect on the quantum-interference pattern.

The diffraction-dependent elements in most of these experimental arrangements are illustrated in Fig. 3(b). To describe this system mathematically via the function H, we need to derive the impulse response function, also known as the point-spread function for optical systems. A typical aperture diameter of $b=1$ cm at a distance $d=1$ m from the crystal output plane yields $b^4/4\lambda d^3<10^{-2}$ using $\lambda=0.5\ \mu$m, guaranteeing the validity of the Fresnel approximation. We therefore proceed with the calculation of the impulse response function in this approximation. Without loss of generality, we now present a two-dimensional (one longi-

tudinal and one transverse) analysis of the impulse response function, extension to three dimensions being straightforward.

Referring to Fig. 3(b), the overall propagation through this system is broken into free-space propagation from the nonlinear-crystal output surface $(x,0)$ to the plane of the aperture (x',d_1), free-space propagation from the aperture plane to the thin lens (x'',d_1+d_2), and finally free-space propagation from the lens to the plane of detection (x_i,d_1+d_2+f), with $i=A,B$. Free-space propagation of a monochromatic spherical wave with frequency ω from $(x,0)$ to (x',d_1) over a distance r is

$$e^{\mathrm{i}(\omega/c)r}=e^{\mathrm{i}(\omega/c)\sqrt{d_1^2+(x-x')^2}}\approx e^{\mathrm{i}(\omega/c)d_1}e^{\mathrm{i}(\omega/2cd_1)(x-x')^2}. \tag{24}$$

The spectral filter is represented mathematically by a function $\mathcal{F}(\omega)$ and the aperture is represented by the function $p(x)$. In the (x',d_1) plane, at the location of the aperture, the impulse response function of the optical system between planes x and x' takes the form

$$h(x',x;\omega)=\mathcal{F}(\omega)\,p(x')e^{\mathrm{i}(\omega/c)d_1}e^{\mathrm{i}(\omega/2cd_1)(x-x')^2}. \tag{25}$$

Also, the impulse response function for the single-lens system from the plane (x',d_1) to the plane (x_i,d_1+d_2+f), as shown in Fig. 3(b), is

$$h(x_i,x';\omega)=e^{\mathrm{i}(\omega/c)(d_2+f)}\exp\left(-\mathrm{i}\frac{\omega x_i^2}{2cf}\left[\frac{d_2}{f}-1\right]\right)e^{-\mathrm{i}\omega x_i x'/cf}. \tag{26}$$

Combining this with Eq. (25) provides

$$\begin{aligned}h(x_i,x;\omega)=\mathcal{F}(\omega)\,e^{\mathrm{i}(\omega/c)(d_1+d_2+f)}\exp\left(-\mathrm{i}\frac{\omega x_i^2}{2cf}\left[\frac{d_2}{f}-1\right]\right)\\ \times e^{\mathrm{i}\omega(x^2/2cd_1)}\int p(x')e^{\mathrm{i}(\omega x'^2/2cd_1)}\\ \times\exp\left(-\mathrm{i}\frac{\omega}{c}x'\left[\frac{x}{d_1}+\frac{x_i}{f}\right]\right)dx',\end{aligned} \tag{27}$$

which is the impulse response function of the entire optical system from the crystal output plane to the detector input plane. We use this impulse response function to determine the transfer function of the system in terms of transverse wave vectors via

$$H(\mathbf{x}_i,\mathbf{q};\omega)=\int d\mathbf{x}\,h(\mathbf{x}_i,\mathbf{x};\omega)\,e^{\mathrm{i}\mathbf{q}\cdot\mathbf{x}}, \tag{28}$$

so that the transfer function explicitly takes the form

$$\begin{aligned}H(\mathbf{x}_i,\mathbf{q};\omega)=\left[e^{\mathrm{i}(\omega/c)(d_1+d_2+f)}\exp\left(-\mathrm{i}\frac{\omega|\mathbf{x}_i|^2}{2cf}\left[\frac{d_2}{f}-1\right]\right)\right.\\ \left.\times e^{-\mathrm{i}(cd_1/2\omega)|\mathbf{q}|^2}\tilde{P}\left(\frac{\omega}{cf}\mathbf{x}_i-\mathbf{q}\right)\right]\mathcal{F}(\omega),\end{aligned} \tag{29}$$

where the function $\tilde{P}[(\omega/cf)\mathbf{x}_i-\mathbf{q}]$ is defined by

$$\tilde{P}\left(\frac{\omega}{cf}\mathbf{x}_i-\mathbf{q}\right)=\int d\mathbf{x}'p(\mathbf{x}')e^{-\mathrm{i}\omega\mathbf{x}'\cdot\mathbf{x}_i/cf}e^{\mathrm{i}\mathbf{q}\cdot\mathbf{x}'}. \tag{30}$$

Using Eq. (29) we can now describe the propagation of the down-converted light from the crystal plane to the detection planes. Since no birefringence is assumed for any material in the system considered to this point, this transfer function is identical for both polarization modes (o,e). In some of the experimental arrangements discussed in this paper, a prism is used to separate the pump field from the SPDC. The alteration of the transfer function H by the presence of this prism is found mathematically to be negligible (see Appendix A) and the effect of the prism is neglected. A parallel set of experiments conducted without the use of a prism further justifies this conclusion (see Sec. III C).

Continuing the analysis in the Fresnel approximation and the approximation that the SPDC fields are quasimonochromatic, we can derive an analytical form for the coincidence-count rate defined in Eq. (13),

$$R(\tau)=R_0[1-V(\tau)], \tag{31}$$

where R_0 is the coincidence rate outside the region of quantum interference. In the absence of spectral filtering

$$\begin{aligned}V(\tau)=\Lambda\left(\frac{2\tau}{LD}-1\right)\mathrm{sinc}\left[\frac{\omega_p^0L^2M^2}{4cd_1}\frac{\tau}{LD}\Lambda\left(\frac{2\tau}{LD}-1\right)\right]\\ \times\tilde{\mathcal{P}}_A\left(-\frac{\omega_p^0LM}{4cd_1}\frac{2\tau}{LD}\mathbf{e}_2\right)\tilde{\mathcal{P}}_B\left(\frac{\omega_p^0LM}{4cd_1}\frac{2\tau}{LD}\mathbf{e}_2\right),\end{aligned} \tag{32}$$

where $D=1/u_o-1/u_e$ with u_j denoting the group velocity for the j-polarized photon $(j=o,e)$, $M=\partial\ln n_e(\omega_p^0/2,\theta_{\mathrm{OA}})/\partial\theta_e$ [10], and $\Lambda(x)=1-|x|$ for $-1\leqslant x\leqslant 1$, and zero otherwise. A derivation of Eq. (32), along with the definitions of all quantities in this expression, is presented in Appendix B. The function $\tilde{\mathcal{P}}_i$ (with $i=A,B$) is the normalized Fourier transform of the squared magnitude of the aperture function $p_i(\mathbf{x})$; it is given by

$$\tilde{\mathcal{P}}_i(\mathbf{q})=\frac{\int\int d\mathbf{y}\,p_i(\mathbf{y})p_i^*(\mathbf{y})\,e^{-\mathrm{i}\mathbf{y}\cdot\mathbf{q}}}{\int\int d\mathbf{y}\,p_i(\mathbf{y})p_i^*(\mathbf{y})}. \tag{33}$$

The profile of the function $\tilde{\mathcal{P}}_i$ within Eq. (32) plays a key role in the results presented in this paper. The common experimental practice is to use extremely small apertures to reach the one-dimensional plane-wave limit. As shown in Eq. (32), this gives $\tilde{\mathcal{P}}_i$ functions that are broad in comparison with Λ so that Λ determines the shape of the quantum interference pattern, resulting in a symmetric triangular dip. The sinc function in Eq. (32) is approximately equal to unity for all practical experimental configurations and therefore plays an insignificant role. On the other hand, this sinc function represents the difference between the familiar one-dimensional model (which predicts $R(\tau)=R_0[1$

$-\Lambda(2\pi/LD-1)]$, a perfectly triangular interference dip) and a three-dimensional model in the presence of a very small on-axis aperture.

Note that for symmetric apertures $|p_i(\mathbf{x})|=|p_i(-\mathbf{x})|$, so from Eq. (33) the functions $\tilde{\mathcal{P}}_i$ are symmetric as well. However, within Eq. (32) the $\tilde{\mathcal{P}}_i$ functions, which are centered at $\tau=0$, are shifted with respect to the function Λ, which is symmetric about $\tau=LD/2$. Since Eq. (32) is the product of functions with different centers of symmetry, it predicts asymmetric quantum-interference patterns, as have been observed in recent experiments [11,12]. When the apertures are wide, the $p_i(\mathbf{x})$ are broad functions that result in narrow $\tilde{\mathcal{P}}_i$, so that the interference pattern is strongly influenced by the shape of the functions $\tilde{\mathcal{P}}_i$. If, in addition, the apertures are spatially shifted in the transverse plane, the $\tilde{\mathcal{P}}_i$ become oscillatory functions that result in sinusoidal modulation of the interference pattern. This can result in a partial inversion of the dip into a peak for certain ranges of the delay τ, as will be discussed subsequently. In short, it is clear from Eq. (32) that $V(\tau)$ can be altered dramatically by carefully selecting the aperture profile.

When SPDC is generated using a finite-bandwidth-pulsed pump field, Eq. (32) becomes

$$V(\tau)=\Lambda\left(\frac{2\tau}{LD}-1\right)\ \mathcal{V}_p(\tau)\times\tilde{\mathcal{P}}_A\left(-\frac{\omega_p^0 LM}{4cd_1}\frac{2\tau}{LD}\mathbf{e}_2\right)\ \tilde{\mathcal{P}}_B\left(\frac{\omega_p^0 LM}{4cd_1}\frac{2\tau}{LD}\mathbf{e}_2\right), \tag{34}$$

where the sinc function in Eq. (32) is simply replaced by $\mathcal{V}_p$, which is given by

$$\mathcal{V}_p(\tau)=\frac{\int d\omega_p\ |\mathcal{E}_p(\omega_p-\omega_p^0)|^2\mathrm{sinc}\left\{\left[D_+L(\omega_p-\omega_p^0)+\frac{\omega_p^0L^2M^2}{4cd_1}\frac{\tau}{LD}\right]\Lambda\left(\frac{2\tau}{LD}-1\right)\right\}}{\int d\omega_p\ |\mathcal{E}_p(\omega_p-\omega_p^0)|^2} \tag{35}$$

with $D_+=1/u_p-\frac{1}{2}(1/u_o+1/u_e)$, where u_j denotes the group velocity for the j-polarized photon ($j=p$, o, and e) and all other parameters are identical to those in Eq. (32). The visibility of the dip in this case is governed by the bandwidth of the pump field.

A. Quantum interference with circular apertures

Of practical interest are the effects of the aperture shape and size, via the function $\tilde{P}(\mathbf{q})$, on polarization quantum-interference patterns. To this end, we consider the experimental arrangement illustrated in Fig. 3(a) in the presence of a circular aperture with diameter b. The mathematical representation of this aperture is given in terms of the Bessel function J_1,

$$\tilde{\mathcal{P}}(\mathbf{q})=2\frac{J_1(b|\mathbf{q}|)}{b|\mathbf{q}|}. \tag{36}$$

For the experiments conducted with cw-pumped SPDC the pump was a single-mode cw argon-ion laser with a wavelength of 351.1 nm and a power of 200 mW. The pump light was delivered to a β-BaB_2O_4 (BBO) crystal with a thickness of 1.5 mm. The crystal was aligned to produce collinear and degenerate Type-II spontaneous parametric down-conversion. The residual pump light was removed from the signal and idler beams with a fused-silica dispersion prism. The collinear beams were then sent through a delay line comprised of a z-cut crystalline quartz element (fast axis orthogonal to the fast axis of the BBO crystal) whose thickness was varied to control the relative optical-path delay between the photons of a down-converted pair. The characteristic thickness of the quartz element was much less than the distance between the crystal and the detection planes, yielding negligible effects on the spatial properties of the SPDC. The photon pairs were then sent to a nonpolarizing beam splitter. Each arm of the polarization intensity interferometer following this beam splitter contained a Glan-Thompson polarization analyzer set to 45°, a convex lens to focus the incoming beam, and an actively quenched Peltier-cooled single-photon-counting avalanche photodiode detector [denoted D_i with $i=A,B$ in Fig. 3(a)]. No spectral filtering was used in the selection of the signal and idler photons for detection. The counts from the detectors were conveyed to a coincidence counting circuit with a 3-ns-coincidence-time window. Corrections for accidental coincidences were not necessary.

The experiments with pulse-pumped SPDC were carried out using the same interferometer as that used in the cw-pumped SPDC experiments, but with ultrafast laser pulses in place of cw laser light. The pump field was obtained by frequency doubling the radiation from an actively mode-locked Ti:sapphire laser, which emitted pulses of light at 830 nm. After doubling, 80-fs pulses (full width at half maximum) were produced at 415 nm, with a repetition rate of 80 MHz and an average power of 15 mW.

For the cw case, the observed normalized coincidence rates (quantum-interference patterns) from a cw-pumped 1.5-mm BBO crystal (symbols), along with the expected theoretical curves (solid), are displayed in Fig. 4 as a function of relative optical-path delay for various values of aperture diameter b placed 1 m from the crystal. Clearly the observed

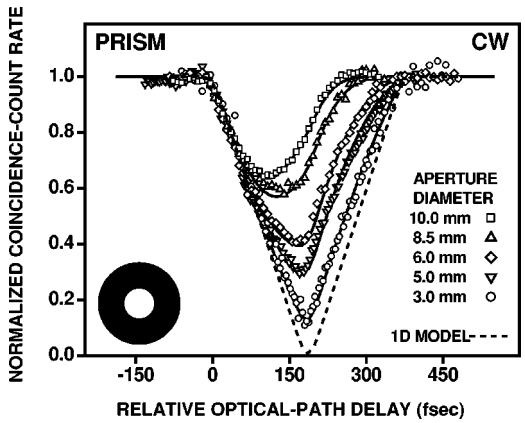

FIG. 4. Normalized coincidence-count rate $R(\tau)/R_0$, as a function of the relative optical-path delay τ, for different diameters of a circular aperture placed 1 m from the crystal. The symbols are the experimental results and the solid curves are the theoretical plots for each aperture diameter. The data were obtained using a 351-nm cw pump and no spectral filters. No fitting parameters are used. The dashed curve represents the one-dimensional (1D) plane-wave theory, which is clearly inadequate for large aperture diameters.

interference pattern is more strongly asymmetric for larger values of b. As the aperture becomes wider, the phase-matching condition between the pump and the generated down-conversion allows a greater range of $(\mathbf{q},\omega)$ modes to be admitted. The $(\mathbf{q},\omega)$ modes that overlap less introduce more distinguishability. This inherent distinguishability, in turn, reduces the visibility of the quantum-interference pattern and introduces an asymmetric shape.

The theoretical plots of the visibility of the quantum-interference pattern at the full-compensation delay $\tau=LD/2$, as a function of the crystal thickness, is plotted in Fig. 5 for various aperture diameters placed 1 m from the crystal. Full visibility is expected only in the limit of extremely thin crystals, or with the use of an extremely small aperture where the one-dimensional limit is applicable. As the crystal thickness increases, the visibility depends more dramatically on the aperture diameter. Similarly, as the aperture diameter increases, the visibility depends more dramatically on the crystal thickness. This is clear from the explicit form of Eq. (32),

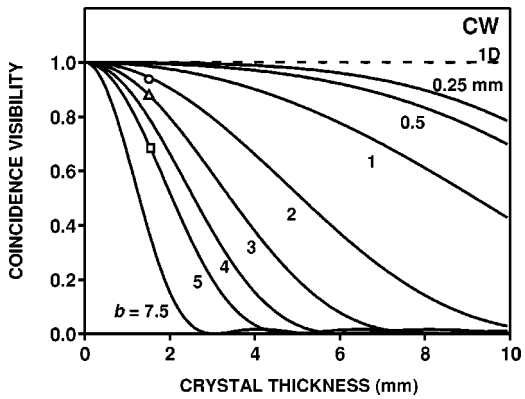

FIG. 5. Solid curves represent theoretical coincidence visibility of the quantum-interference pattern for cw SPDC as a function of crystal thickness, for various circular-aperture diameters b placed 1 m from the crystal. The dashed line represents the one-dimensional (1D) plane-wave limit of the multiparameter formalism. Visibility is calculated for a relative optical-path delay $\tau=LD/2$. The symbols represent experimental data collected using a 1.5-mm-thick BBO crystal, and selected aperture diameters b of 2 mm (circle), 3 mm (triangle), and 5 mm (square), as indicated on the plot.

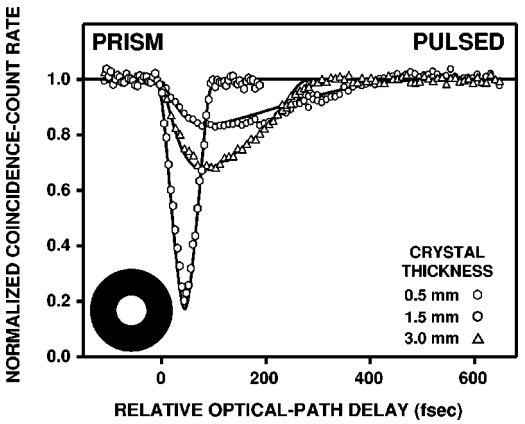

FIG. 6. Normalized coincidence-count rate, as a function of the relative optical-path delay τ, for 0.5-mm-, 1.5-mm-, and 3-mm-thick BBO crystals as indicated in the plot. A 5-mm circular aperture was placed 1 m from the crystal. The symbols are the experimental results reported in Refs. [11,12], while the solid curves are the corresponding theoretical plots associated with the multiparameter formalism presented here and in Ref. [11]. The data were obtained using an 80-fs-pulsed pump centered at 415 nm and no spectral filters. No fitting parameters are used. (Adapted from Refs. [11,12].)

$$V(\tau)=4\,\mathrm{sinc}\left[\frac{\omega_p^0 L^2 M^2}{8cd_1}\right]\left|\frac{J_1\left(\frac{\omega_p^0 M}{4cd_1}Lb\right)}{\frac{\omega_p^0 M}{4cd_1}Lb}\right|^2 \tag{37}$$

for $\tau=LD/2$ and a circular aperture profile for which we used Eq. (36). It is apparent that Eq. (37) depends on the product Lb. The experimentally observed visibility for various aperture diameters, using the 1.5-mm-thick BBO crystal employed in our experiments (symbols in Fig. 5), is consistent with the theory.

If the pump field in Fig. 3 is pulsed, then there are additional limitations on the visibility that emerge as a result of the broad spectral bandwidth of the pump field [11–14]. The validity of our analysis in the case of pulse-pumped SPDC has been confirmed in our earlier work [11], the results of which are reproduced in Fig. 6. This figure is presented here expressly to provide a comparison with Fig. 12, showing that asymmetry in the quantum-interference pattern is obtained whether a prism or a dichroic mirror is used to remove the femtosecond-pulsed pump. The asymmetry of the interference pattern for increasing crystal thickness is more visible in the pulsed than in the cw regime. With respect to visibilities, Fig. 7 shows a plot for the pulsed-pump case similar to Fig. 5 for the cw case.

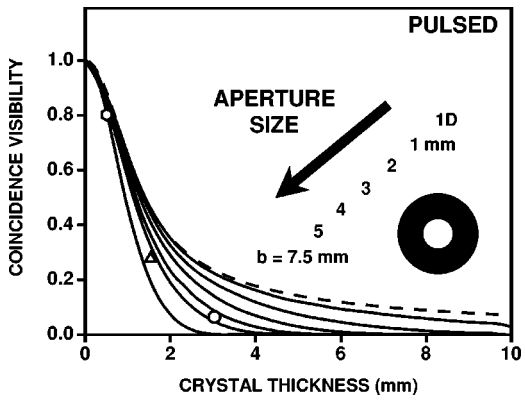

FIG. 7. Solid curves represent theoretical coincidence visibility of the quantum-interference pattern for pulsed SPDC as a function of crystal thickness, for various circular-aperture diameters b placed 1 m from the crystal. Visibility is calculated for a relative optical-path delay $\tau = LD/2$. The dashed curve represents the one-dimensional (1D) plane-wave limit of the multiparameter formalism. The symbols represent experimental data collected using a 3.0-mm aperture and BBO crystals of thickness 0.5 mm (hexagon), 1.5 mm (triangle), and 3.0 mm (circle). Comparison should be made with Fig. 5 for the cw SPDC.

B. Quantum interference with slit apertures

For the majority of quantum-interference experiments involving relative optical-path delay, circular apertures are the norm. In this section we consider the use of a vertical slit aperture to investigate the transverse symmetry of the generated photon pairs. Since the experimental arrangement of Fig. 3(a) remains identical except for the aperture, Eq. (21) still holds and $p(\mathbf{x})$ takes the explicit form

$$\tilde{\mathcal{P}}(\mathbf{q}) = \frac{\sin(b\,\mathbf{e}_1\cdot\mathbf{q})}{b\,\mathbf{e}_1\cdot\mathbf{q}}\,\frac{\sin(a\,\mathbf{e}_2\cdot\mathbf{q})}{a\,\mathbf{e}_2\cdot\mathbf{q}}. \tag{38}$$

The data shown by squares in Fig. 8 are the observed normalized coincidence rates for a cw-pumped 1.5-mm BBO in the presence of a vertical slit aperture with $a = 7$ mm and $b = 1$ mm. The quantum-interference pattern is highly asymmetric and has low visibility, and indeed is similar to that obtained using a wide circular aperture (see Fig. 4). The solid curve is the theoretical quantum-interference pattern expected for the vertical slit aperture used.

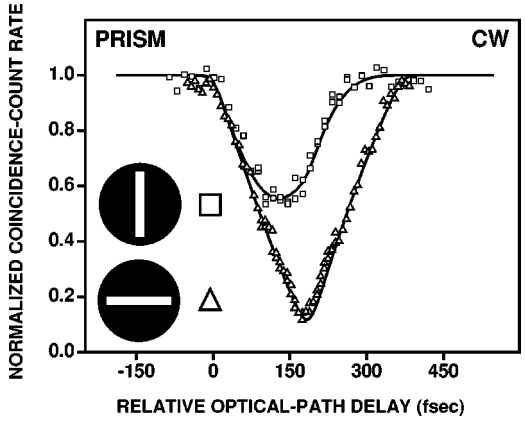

FIG. 8. Normalized coincidence-count rate as a function of the relative optical-path delay for a 1-mm × 7-mm horizontal slit (triangles). The data were obtained using a 351-nm cw pump and no spectral filters. Experimental results for a vertical slit are indicated by squares. Solid curves are the theoretical plots for the two orientations.

In order to investigate the transverse symmetry, the complementary experiment has also been performed using a horizontal slit aperture. For the horizontal slit, the parameters a and b in Eq. (38) are interchanged so that $a = 1$ mm and $b = 7$ mm. The data shown by triangles in Fig. 8 are the observed normalized coincidence rates for a cw-pumped 1.5-mm BBO in the presence of this aperture. The most dramatic effect observed is the symmetrization of the quantum-interference pattern and the recovery of the high visibility, despite the wide aperture along the horizontal axis. A practical benefit of such a slit aperture is that the count rate is increased considerably, which is achieved by limiting the range of transverse wave vectors along the optical axis of the crystal to induce indistinguishability and allowing a wider range along the orthogonal axis to increase the collection efficiency of the SPDC photon pairs. This finding is of significant value, since a high count rate is required for many applications of entangled photon pairs and, indeed, many researchers have suggested more complex means of generating high-flux photon pairs [15].

Noting that the optical axis of the crystal falls along the vertical axis, these results verify that the dominating portion of distinguishability lies, as expected, along the optical axis. The orthogonal axis (horizontal in this case) provides a negligible contribution to distinguishability, so that almost full visibility can be achieved despite the wide aperture along the horizontal axis.

The optical axis of the crystal in the experimental arrangements discussed above is vertical with respect to the lab frame. This coincides with the polarization basis of the down-converted photons. To stress the independence of these two axes, we wish to make the symmetry axis for the spatial distribution of SPDC distinct from the polarization axes of the down-converted photons. One way of achieving this experimentally is illustrated in Fig. 9(a). Rather than using a simple BBO crystal we incorporate two half-wave plates, one placed before the crystal and aligned at 22.5° with respect to the vertical axis of the laboratory frame, and the other after the crystal and aligned at $-22.5°$. The BBO crystal is rotated by 45° with respect to the vertical axis of the laboratory frame. Consequently, SPDC is generated in a special distribution with a 45°-rotated axis of symmetry, while keeping the polarization of the photons aligned with the horizontal and the vertical axes. Rotated-slit-aperture experiments with cw-pumped SPDC, similar to those presented in Fig. 8, were carried out using this arrangement. The results are shown in Fig. 9(b). The highest visibility in the quantum-interference pattern occurred when the vertical slit was rotated $-45°$ (triangles), while the lowest and the most asymmetric pattern occurred when the vertical slit aperture was rotated $+45°$ (squares). This verifies that the effect of axis selection is solely due to the spatiotemporal distribution

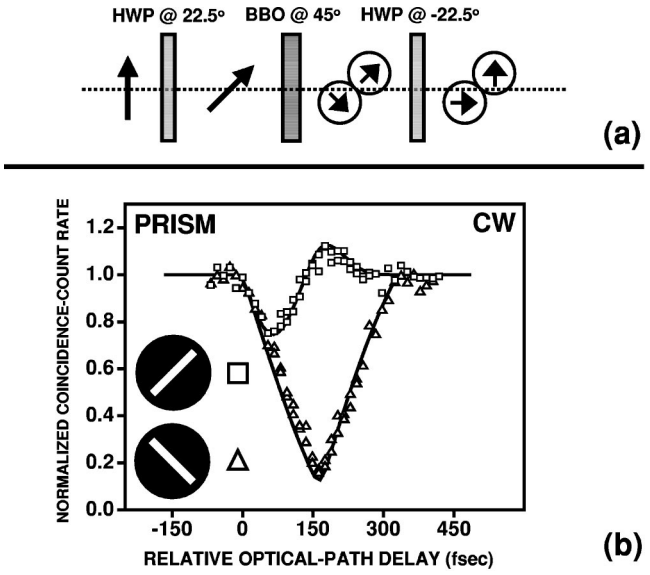

FIG. 9. (a) A half-wave plate at 22.5° rotation, and another half-wave plate at $-22.5°$ rotation are placed before and after the BBO crystal in Fig. 3(a), respectively. This arrangement results in SPDC polarized along the horizontal-vertical axes and the axis of symmetry rotated 45° with respect to the vertical axis. (b) Normalized coincidence-count rate from cw-pumped SPDC as a function of the relative optical-path delay for a 1-mm $\times$ 7-mm vertical slit rotated $-45°$ (triangles). Experimental results for a vertical slit rotated $+45°$ are indicated by squares. Solid curves are the theoretical plots for the two orientations.

of SPDC, and not related to any birefringence or dispersion effects associated with the linear elements in the experimental arrangement.

C. Quantum interference with increased acceptance angle

A potential obstacle for accessing a wider range of transverse wave vectors is the presence of dispersive elements in the optical system. One or more dispersion prisms, for example, are often used to separate the intense pump field from the down-converted photons [16]. As discussed in Appendix A, the finite angular resolution of the system aperture and collection optics can, in certain limits, cause the prism to act as a spectral filter.

To increase the limited acceptance angle of the detection system and more fully probe the multiparameter interference features of the entangled-photon pairs, we carry out experiments using the alternate setup shown in Fig. 10. Note that a dichroic mirror is used in place of a prism. Moreover, the effective acceptance angle is increased by reducing the distance between the crystal and the aperture plane. This allows us to access a greater range of transverse wave vectors with our interferometer, facilitating the observation of the effects discussed in Secs. III A and III B without the use of a prism.

Using this experimental arrangement, we repeated the circular-aperture experiments, the results of which were presented in Fig. 4. Figure 11 displays the observed quantum-interference patterns (normalized coincidence rates) from a cw-pumped 1.5-mm BBO crystal (symbols) along with the

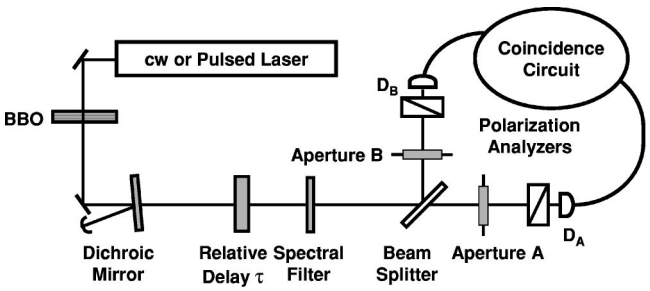

FIG. 10. Schematic of alternate experimental setup for observation of quantum interference using cw-pumped Type-II collinear SPDC. The configuration illustrated here makes use of a dichroic mirror in place of the prism used in Fig. 3(a), thereby admitting greater acceptance of the transverse-wave components. The dichroic mirror reflects the pump wavelength while transmitting a broad wavelength range that includes the bandwidth of the SPDC. The single aperture shown in Fig. 3(a) is replaced by separate apertures placed equal distances from the beam splitter in each arm of the interferometer.

expected theoretical curves (solid) as a function of relative optical-path delay for various values of the aperture diameter b placed 750 mm from the crystal. For the data on the curve with the lowest visibility (squares), the limiting apertures in the system were determined not by the irises as shown in Fig. 11, but by the dimensions of the Glan-Thompson polarization analyzers, which measure 7 mm across.

Similar experiments were conducted with pulse-pumped SPDC in the absence of prisms. The resulting quantum-interference patterns are shown as symbols in Fig. 12. The observed quantum-interference patterns (normalized coincidence rates) from a 1.5-mm BBO crystal (symbols) along with the expected theoretical curves (solid) as a function of relative optical-path delay for two values of the aperture di-

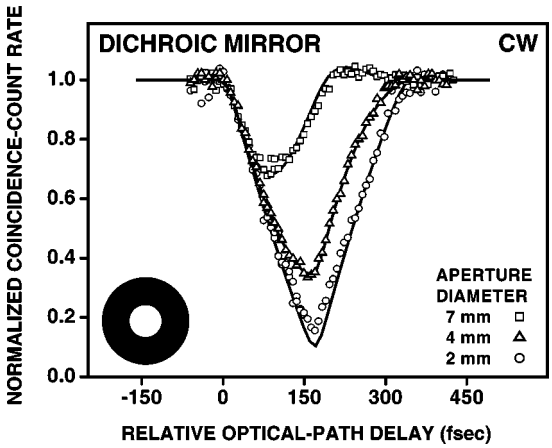

FIG. 11. Normalized coincidence-count rate as a function of the relative optical-path delay τ, for different diameters of an aperture that is circular in the configuration of Fig. 10. The symbols are the experimental results and the solid curves are the theoretical plots for each aperture diameter. The data were obtained using a 351-nm cw pump and no spectral filters. No fitting parameters are used. The behavior of the interference pattern is similar to that observed in Fig. 4; the dependence on the diameter of the aperture is slightly stronger in this case.

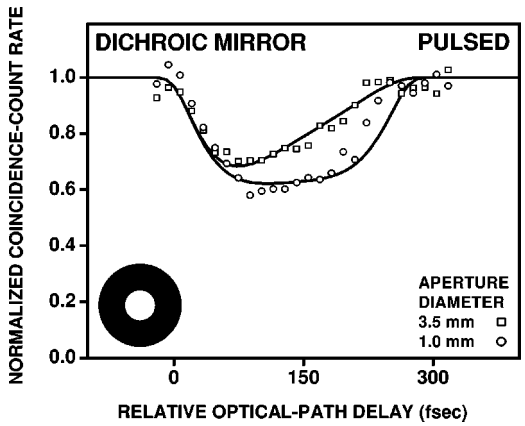

FIG. 12. Normalized coincidence-count rate as a function of the relative optical-path delay, for different diameters of an aperture that is circular in the configuration of Fig. 10. The symbols are the experimental results and the solid curves are the theoretical plots for each aperture diameter. The data were obtained using an 80-fs pulsed pump centered at 415 nm and no spectral filters. In contrast to the results presented in Fig. 6, a dichroic mirror was used to remove the femtosecond pump. No fitting parameters are used. Analogous results for cw-pumped down-conversion are shown in Figs. 4 and 11.

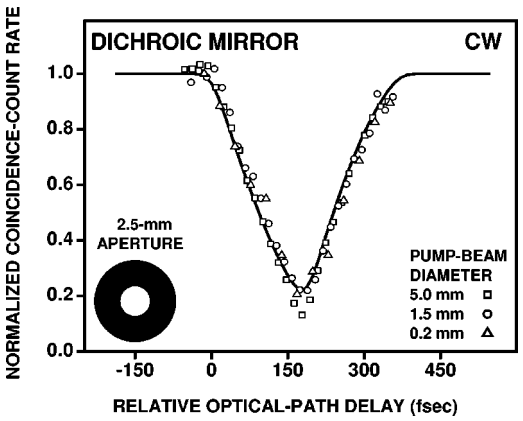

FIG. 13. Normalized coincidence-count rate as a function of the relative optical-path delay, for different diameters of the pump beam in the configuration of Fig. 10. The symbols are the experimental results and the solid curve is the theoretical plot of the quantum-interference pattern for an infinite plane-wave pump. The data were obtained using a 351-nm cw pump and no spectral filters. The circular aperture in the optical system for the down-converted light was 2.5 mm at a distance of 750 mm. No fitting parameters are used.

ameter *b* placed 750 mm from the crystal. The solid curves are the interference patterns calculated by using the model given in Sec. II, again assuming a Gaussian spectral profile for the pump. Comparing Fig. 12 with Fig. 6, we note that the asymmetry in the quantum-interference patterns is maintained irrespective of whether a prism or a dichroic mirror is used to remove the femtosecond pump. This is consistent with the multiparameter entangled nature of SPDC.

An experimental study directed specifically toward examining the role of the prism, which is used to remove the residual pump light, in a similar quantum-interference experiment has recently been presented in Ref. [17]. In that work, the authors carried out a set of experiments both with and without prisms. They reported that the interference patterns observed with a prism in the apparatus are asymmetric, while those obtained in the absence of such a prism are symmetric. The authors claim that the asymmetry of the quantum-interference pattern is an artifact of the presence of the prism. In contrast to the conclusions of that study, we show that asymmetrical patterns are, in fact, observed in the absence of a prism (see Fig. 12). Indeed, our theory and experiments show that interference patterns become symmetric when narrow apertures are used, either in the absence or in the presence of a prism. This indicates conclusively that transverse effects are responsible for asymmetry in the interference pattern in the present experiment, which may not have been the case in previous experiments.

D. Pump-field diameter effects

The examples of the pump field we have considered are all plane waves. In this section, and in the latter part of Appendix B, we demonstrate the validity of this assumption under our experimental conditions and find a limit where this assumption is no longer valid. To demonstrate the independence of the interference pattern on the size of the pump, we placed a variety of apertures directly at the front surface of the crystal. Figure 13 shows the observed normalized coincidence rates from a cw-pumped 1.5-mm BBO crystal (symbols) as a function of the relative optical-path delay for various values of pump beam diameter. The acceptance angle of the optical system for the down-converted light is determined by a 2.5-mm aperture at a distance of 750 mm from the crystal. The theoretical curve (solid) corresponds to the quantum-interference pattern for an infinite plane-wave pump. Figure 14 shows similar plots as in Fig. 13 in the presence of a 5-mm aperture in the optical system for the down-converted light. The typical value of the pump beam diameter in quantum-interference experiments is 5 mm. The experimental results from a 5-mm-, 1.5-mm-, and 0.2-mm-diameter pump all lie within experimental uncertainty, and are practically identical except for the extreme reduction in count rate due to the reduced pump intensity.

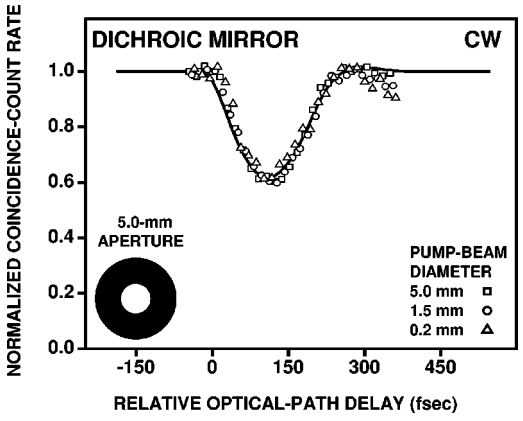

FIG. 14. Plots similar to those in Fig. 13 in the presence of a 5.0-mm circular aperture in the optical system for the down-converted light.

This behavior of the interference pattern suggests that the dependence of the quantum-interference pattern on the diameter of the pump beam is negligible within the limits considered in this work. Indeed, if the pump diameter is comparable to the spatial walk-off of the pump beam within the nonlinear crystal, then the plane-wave approximation is not valid and the proper spatial profile of the pump beam must be considered in Eq. (23). For the 1.5-mm BBO used in our experiments this limit is ≈ 70 μm, which is smaller than any aperture we could use without facing prohibitively low count rates.

E. Shifted-aperture effects

In the work presented thus far, the optical elements in the system are placed concentrically about the longitudinal (z) axis. In this condition, the sole aperture before the beam splitter, as shown in Fig. 3(a), yields the same transfer function as two identical apertures placed in each arm after the beam splitter, as shown in Fig. 10. In this section we show that the observed quantum-interference pattern is also sensitive to a *relative shift* of the apertures in the transverse plane. To account for this, we must include an additional factor in Eq. (32),

$$\cos\left[\frac{\omega_p LM}{4cd_1}\frac{2\tau}{LD}\mathbf{e}_2\cdot(\mathbf{s}_A-\mathbf{s}_B)\right], \tag{39}$$

where $\mathbf{s}_i$ (with $i=A,B$) is the displacement of each aperture from the longitudinal (z) axis. This extra factor provides yet another degree of control on the quantum-interference pattern for a given aperture form.

1. Quantum interference with shifted-slit apertures

First, we revisit the case of slit apertures, discussed above in Sec. III B. Using the setup shown in Fig. 10, we placed identically oriented slit apertures in each arm of the interferometer, which can be physically shifted up and down in the transverse plane. A spatially shifted aperture introduces an extra phase into the $\tilde{\mathcal{P}}(\mathbf{q})$ functions, which, in turn, results in the sinusoidal modulation of the quantum-interference pattern as shown in Eq. (39) above.

The two sets of data shown in Fig. 15 represent the observed normalized coincidence rates for a cw-pumped 1.5-mm BBO crystal in the presence of identical apertures placed without shift in each arm as shown in Fig. 10. The triangular points correspond to the use of 1-mm $\times$ 7-mm horizontal slits. The square points correspond to the same apertures rotated 90° to form vertical slits. Since this configuration, as shown in Fig. 10, accesses a wider range of acceptance angles, the dimensions of the other optical elements become relevant as effective apertures in the system. Although the apertures themselves are aligned symmetrically, an effective vertical shift of $|\mathbf{s}_A-\mathbf{s}_B|=1.6$ mm is induced by the relative displacement of the two polarization analyzers. The solid curves in Fig. 15 are the theoretical plots for the two aperture orientations. Note that as in the experiments described in Sec. III B, the horizontal slits give a high visibility interference pattern, and the vertical slits give an asymmetric pattern with low visibility, even in the absence of a prism. Note further that the cosine modulation of Eq. (39) results in peaking of the interference pattern when the vertical slits are used.

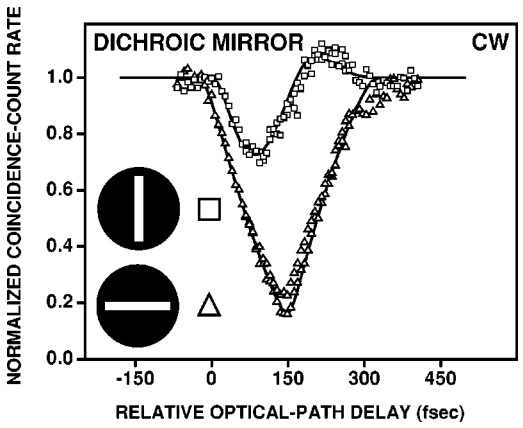

FIG. 15. Normalized coincidence-count rate as a function of the relative optical-path delay for identical 1-mm $\times$ 7-mm horizontal slits placed in each arm in the configuration of Fig. 10 (triangles). The data were obtained using a 351-nm cw pump and no spectral filters. Experimental results are also shown for two identical 1-mm $\times$ 7-mm vertical slits, but shifted with respect to each other by 1.6 mm along the long axis of the slit (squares). Solid curves are the theoretical plots for the two orientations.

2. Quantum interference with shifted-ring apertures

Given the experimental setup shown in Fig. 10 with an annular aperture in arm A and a 7-mm circular aperture in arm B, we obtained the quantum-interference patterns shown in Fig. 16. The annular aperture used had an outer diameter of $b=4$ mm and an inner diameter of $a=2$ mm, yielding an aperture function

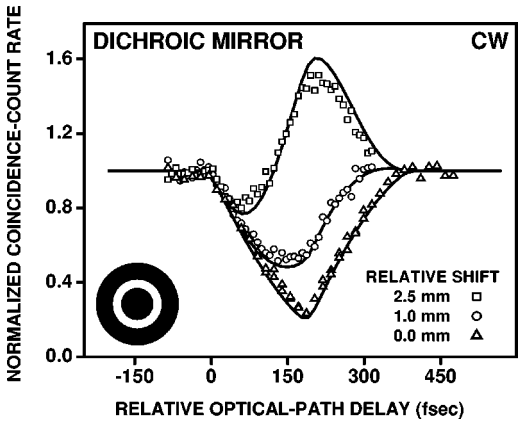

FIG. 16. Normalized coincidence-count rate as a function of the relative optical-path delay, for an annular aperture (internal and external diameters of 2 and 4 mm, respectively) in one of the arms of the interferometer in the configuration of Fig. 10. A 7-mm circular aperture is placed in the other arm. The data were obtained using a 351-nm cw pump and no spectral filters. The symbols are experimental results for different relative shifts of the annulus along the direction of the optical axis of the crystal (vertical). The solid curves are the theoretical plots without any fitting parameters.

$$\tilde{\mathcal{P}}_A(\mathbf{q}) = \frac{2}{b-a}\left[\frac{J_1(b|\mathbf{q}|)}{|\mathbf{q}|} - \frac{J_1(a|\mathbf{q}|)}{|\mathbf{q}|}\right]. \tag{40}$$

The symbols give the experimental results for various values of the relative shift $|\mathbf{s}_A - \mathbf{s}_B|$, as denoted in the legend. Note that as in the case of the shifted slit, $V(\tau)$ becomes negative for certain values of the relative optical-path delay (τ), and the interference pattern displays a peak rather than the familiar triangular dip usually expected in this type of experiment.

IV. CONCLUSION

In summary, we observe that the multiparameter entangled nature of the two-photon state generated by SPDC allows transverse spatial effects to play a role in polarization-based quantum-interference experiments. The interference patterns generated in these experiments are, as a result, governed, in part, by the profiles of the apertures in the optical system, which admit wave vectors in specified directions. Including a finite bandwidth for the pump field strengthens this dependence on the aperture profiles, clarifying why the asymmetry was first observed in the ultrafast regime [11]. The phenomenological analysis provided in our earlier paper [12] was confined to a 1D theoretical construct and, as such, needed to invoke distinguishability to characterize the data. It is gratifying that the multiparameter theory presented here is capable of fitting both cw and ultrafast SPDC quantum-interference data, taking into account the full properties of the down-conversion process and obviating the need for a phenomenological construct. The effect of the pump-beam diameter on the quantum-interference pattern has also been shown to be negligible for a typical range of pump diameter values used in similar experimental arrangements. Moreover, the multiparameter formalism presented here is suitable for characterizing SPDC from a nonlinear medium with inhomogeneous nonlinearity; this has been explicitly demonstrated for a cascade of two nonlinear crystals separated by an air gap [18].

In contrast to the usual single-direction polarization-entangled state, the wide-angle polarization-entangled state offers a richness that can be exploited in a variety of applications involving quantum-information processing.

ACKNOWLEDGMENTS

This work was supported by the National Science Foundation, the David and Lucile Packard Foundation, and the Defense Advanced Research Projects Agency. The authors thank A. F. Abouraddy and M. C. Booth for valuable suggestions.

APPENDIX A: EFFECT OF PRISM ON SYSTEM TRANSFER FUNCTION

A complete mathematical analysis was carried out to analyze the effects of the prism on the system transfer function under the standard paraxial approximation [16]. This appendix sets forth the physical understanding of this analysis, which is rather lengthy and is therefore not provided here.

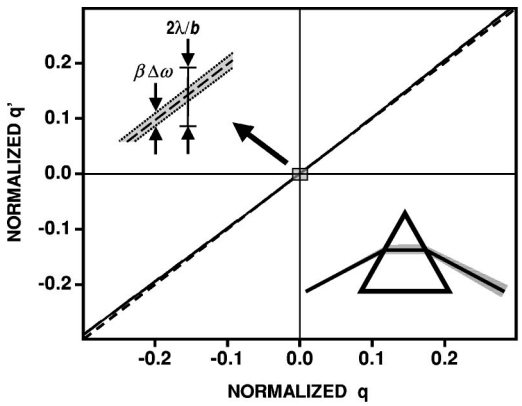

FIG. 17. A plot of Eq. (A2), the relation between the magnitudes of the transverse wave vectors entering ($\mathbf{q}$) and exiting ($\mathbf{q}'$) a fused-silica prism with an apex angle of 60° (see inset at lower right). The range of transverse wave vectors allowed by the optical system in our experiments lies completely within the area included in the tiny box at the center of the plot. The upper left inset shows details of this central region. The dashed curve is a line with unity slope representing the $|\mathbf{q}'| = |\mathbf{q}|$ map. The dotted lines denote the deviation from this mapping arising from the spectral bandwidth ($\Delta\omega$) of the incident light beam. As long as the width of the shaded area, which denotes the angular dispersion of the prism, is smaller than the angular resolution ($2\lambda/b$) of the aperture-lens combination, the effect of the prism is negligible.

We present a mathematical analysis of the effect of the prism used in some of the experiments presented above on the spatiotemporal distribution of SPDC. We begin by assuming that the central wavelength for down-conversion is aligned at the minimum deviation angle ϕ_0, so that the input and the output angles of the prism are equal. The optical axis (z) used in the calculation of the system transfer function follows these angles as shown in the inset of Fig. 17. Within the paraxial and quasimonochromatic field approximations the prism is represented by a mapping of each $(\mathbf{q},\omega)$ mode to a $(\mathbf{q}',\omega)$ mode. Using Snell's Law, the relation between $\mathbf{q}$ and $\mathbf{q}'$ at a given frequency ω is dictated by

$$\mathcal{S}(\mathbf{q},\mathbf{q}') + \mathcal{S}(\mathbf{q}',\mathbf{q}) = n^2(\omega)\sin(\alpha), \tag{A1}$$

where α is the apex angle of the prism. The function $\mathcal{S}$ is given by

$$\mathcal{S}(\mathbf{q},\mathbf{q}') = \left[\sin(\phi_0) + \frac{\cos(\phi_0)\,c}{\omega}\mathbf{q}\cdot\mathbf{e}_1 - \frac{\sin(\phi_0)c^2}{2\omega^2}|\mathbf{q}\cdot\mathbf{e}_1|^2\right] \times\left[n^2(\omega) - \sin(\phi_0)^2 - \frac{\sin(2\phi_0)\,c}{\omega}\mathbf{q}'\cdot\mathbf{e}_1 - \frac{\cos(2\phi_0)c^2}{\omega^2}|\mathbf{q}'\cdot\mathbf{e}_1|^2\right]^{1/2}. \tag{A2}$$

Figure 17 shows a plot of $\mathbf{q}'$ as a function of $\mathbf{q}$. Plotting this curve for various frequencies ω produces no deviation visible within the resolution of the printed graph. The small box at the center of the plot highlights the range of transverse wave vectors limited by the acceptance angle of the optical

system used in the above experiments. The dashed line is the $|\mathbf{q}'|=|\mathbf{q}|$ curve with unity slope.

We now consider a linear expansion in frequencies and transverse wave vectors of the above-mentioned mapping of a $(\mathbf{q},\omega)$ mode to a $(\mathbf{q}',\omega)$ mode in the form

$$\mathbf{q}'\cdot\mathbf{e}_1 \approx -\mathbf{q}\cdot\mathbf{e}_1+\beta\frac{\omega_p^0}{c}\left(\omega-\frac{\omega_p^0}{2}\right),$$

$$\mathbf{q}'\cdot\mathbf{e}_2 \approx \mathbf{q}\cdot\mathbf{e}_2, \tag{A3}$$

where the negative sign multiplying $\mathbf{q}\cdot\mathbf{e}_1$ indicates that a ray of light at the input face of the prism with a small deviation in one direction is mapped to a ray of light at the output face with a corresponding deviation in the opposite direction (see Eq. (16) in Sec. 4.7.2 of Ref. [19]). The parameter β corresponds to the angular dispersion parameter of the prism [19] with the explicit form given by

$$\beta=\frac{\sin\alpha}{\cos\phi_0\cos(\alpha/2)}\frac{dn}{d\omega}. \tag{A4}$$

To find the range of aperture diameters b, where the effect of the prism can be considered negligible, we need to compare the angular resolution of the aperture-lens combination at the detection plane to the angular dispersion of the prism. A system with an infinite aperture and an infinite lens maps each wave vector into a distinct point at the detection plane. In practice, of course, a finite aperture limits the angular resolution of the system at the detection plane to the order of $2\lambda/b$, where λ is the central wavelength of the down-converted light and b is the diameter of the aperture. Now, the prism maps each frequency into a distinct wave vector. The angular dispersion of the prism is on the order of $\beta\Delta\omega$ where $\Delta\omega$ is the bandwidth of the incident light beam. If the angular dispersion of the prism is less than the angular resolution of the combined aperture and lens, the dispersive properties of the prism have negligible effect on the quantum-interference pattern.

For an SPDC bandwidth of 10 nm around a central wavelength of 702 nm and a value of β given by 5.8×10^{-18} s (calculated from the material properties of fused silica), the effect of the angular dispersion introduced by the prism on the experiments presented in this paper can be safely neglected for aperture diameters less than 20 mm. For aperture diameters in the vicinity of this value and higher, the effect on the quantum-interference pattern is a spectral-filter-like smoothing of the edges. The chromatic dispersion experienced by the down-converted light when propagating through such dispersive elements has already been examined [14]; the dispersiveness of the material must be an order of magnitude higher than the values used in the experiments considered here to have a significant effect on the down-converted light.

We conclude that the transfer function of the system, provided in Eq. (29), is not affected by the presence of the prism. Moreover, the results discussed in Secs. III A, III B, and III C experimentally confirm that the effect of the prism on the quantum-interference pattern is negligible in comparison with other spatial and spectral effects.

APPENDIX B: DERIVATION OF VISIBILITY IN EQ. (32)

The purpose of this appendix is to derive Eq. (32) using Eqs. (13), (21), and (29). To obtain an analytical solution within the Fresnel approximation we assume quasimonochromatic fields and perform an expansion in terms of a small angular frequency spread (ν) around the central angular frequency ($\omega_p^0/2$) associated with degenerate down-conversion, and small transverse components $|\mathbf{q}|$ with respect to the total wave vector $\mathbf{k}_j$ for collinear down-conversion. In short, we use the fact that $|\nu|\ll\omega_p^0/2$, with $\nu=\omega-\omega_p^0/2$, and $|\mathbf{q}|^2\ll|\mathbf{k}|^2$. In these limits we obtain

$$\kappa_o(\omega,\mathbf{q})\approx K_o+\frac{\omega-\omega_p^0/2}{u_o}-\frac{|\mathbf{q}|^2}{2K_o} \tag{B1}$$

$$\kappa_e(\omega,\mathbf{q})\approx K_e-\frac{\omega-\omega_p^0/2}{u_e}-\frac{|\mathbf{q}|^2}{2K_e}+M\mathbf{e}_2\cdot\mathbf{q}, \tag{B2}$$

where the explicit forms for K_j, u_j $j=o,e$, and $M\mathbf{e}_2$ are [10]

$$K_j=|\mathbf{k}_j(\omega,\mathbf{q})|_{\omega_p^0/2,\mathbf{q}=0},\qquad \frac{1}{u_j}=\left.\frac{\partial\kappa_j(\omega,\mathbf{q})}{\partial\omega}\right|_{\omega_p^0/2,\mathbf{q}=0},$$

$$M\mathbf{e}_2=\left.\frac{|\mathbf{k}_e|\nabla_{\mathbf{q}}|\mathbf{k}_e|}{\kappa_e}\right|_{\omega_p^0/2,\mathbf{q}=0},$$

$$M=\left.\frac{\partial\ln n_e(\omega,\theta_e)}{\partial\theta_e}\right|_{\omega_p^0/2,\theta_e=\theta_{\mathrm{OA}}}. \tag{B3}$$

Using the results in Eqs. (B1), (B2), and (B3) we can now provide an approximate form for Δ, which is the argument of the sinc function in Eq. (21), as

$$\Delta\approx -D\nu+\frac{2c|\mathbf{q}|^2}{\omega_p^0}+M\mathbf{e}_2\cdot\mathbf{q}, \tag{B4}$$

where $D=1/u_o-1/u_e$.

Using this approximate form for Δ in the integral representation of $\mathrm{sinc}(x)$

$$\mathrm{sinc}\left(\frac{L\Delta}{2}\right)e^{-iL\Delta/2}=\int_{-L}^{0}dz\,e^{-iz\Delta}, \tag{B5}$$

with the assumption that $L\ll d_1$, we obtain Eq. (31) with

$$R_0=\int d\nu\int_{-L}^{0}dz\,e^{-iD\nu z}\int_{-L}^{0}dz'\,e^{iD\nu z'}\,\mathcal{J}_0(z,z'), \tag{B6}$$

$$V(\tau)=\frac{1}{R_0}\int d\nu\, e^{-2i\tau\nu}\int_{-L}^{0}dz\, e^{-iD\nu z}\times\int_{-L}^{0}dz'\, e^{-iD\nu z'}\,\mathcal{J}_V(z,z'),\tag{B7}$$

where the functions

$$\mathcal{J}_0(z,z')=\left(\frac{\omega_p^0}{2cd_1}\right)^2\exp\left[-i\frac{\omega_p^0}{8cd_1}M^2(z^2-z'^2)\right]\times\tilde{\mathcal{P}}_A\left[\frac{\omega_p^0}{4cd_1}M(z-z')\mathbf{e}_2\right]\times\tilde{\mathcal{P}}_B\left[-\frac{\omega_p^0}{4cd_1}M(z-z')\mathbf{e}_2\right],\tag{B8}$$

$$\mathcal{J}_V(z,z')=\left(\frac{\omega_p^0}{2cd_1}\right)^2\exp\left[-i\frac{\omega_p^0}{8cd_1}M^2(z^2-z'^2)\right]\times\tilde{\mathcal{P}}_A\left[\frac{\omega_p^0}{4cd_1}M(z+z')\mathbf{e}_2\right]\times\tilde{\mathcal{P}}_B\left[-\frac{\omega_p^0}{4cd_1}M(z+z')\mathbf{e}_2\right]\tag{B9}$$

are derived by carrying out the integrations over the variables **x** and **q**.

Performing the remaining integrations leads us to Eq. (32). This equation allows robust and rapid numerical simulations of quantum-interferometric measurement to be obtained. For the simulations provided in this work with pump wavelength of 351 nm, the calculated values of M and D are 0.0711 and 248 fs/mm, respectively. Similarly, given a pump wavelength of 415 nm, we compute $M=0.0723$ and $D=182$ fs/mm.

In the case of Type-I SPDC, both photons of a generated pair have ordinary polarization. Consequently, the vector $M\mathbf{e}_2$ does not appear in the expansions of the wave vectors, unless the pump field itself has transverse wave-vector components. Since the $|\mathbf{q}|^2$ term in the expansion of Δ, as given in Eq. (B4), is smaller than $M\mathbf{e}_2\cdot\mathbf{q}$ within the paraxial approximation, similar effects in Type-I quantum-interferometric measurements are expected to be smaller given the same aperture size.

If the pump field is not a monochromatic plane wave, but rather has finite spectral bandwidth and transverse extent, the function Δ defined after Eq. (8) can be approximated by

$$\Delta\approx -D\nu+D_+\nu_p+\frac{c}{\omega_p^0}[2|\mathbf{q}|^2+|\mathbf{q}_p|^2]+M\mathbf{e}_2\cdot\mathbf{q}+\left(M_p-\frac{M}{2}\right)\mathbf{e}_2\cdot\mathbf{q}_p,\tag{B10}$$

where $D_+=1/u_p-\frac{1}{2}(1/u_o+1/u_e)$, u_p is the pump group velocity in the nonlinear medium, $\nu_p=\omega_p-\omega_p^0$ is the deviation of the angular pump frequency, $\mathbf{q}_p$ is the pump transverse wave vector in the crystal, and M_p is the spatial walk-off for the pump beam. The second term in Eq. (B10), which depends on the bandwidth of the pump field, is negligible if the pump field is monochromatic. The last term in Eq. (B10), which depends on the transverse wave vector of the pump field, is negligible if the condition

$$\frac{\left|\left(M_p-\frac{M}{2}\right)\right|L}{a}\ll 1\tag{B11}$$

is satisfied, where a is a characteristic width of the pump beam at the crystal. For a 1.5-mm BBO crystal pumped by a 351-nm laser, $M=0.0711$ and $M_p=0.0770$, so that the pump diameter would have to be less than or equal to 70 μm to invalidate the plane-wave approximation. If such spatial walk-off is neglected, the governing limit, arising from the remaining contribution from diffraction [fourth term in Eq. (B10)], is found in Ref. [20] to be about 10 μm for the experimental arrangement presented in this work. Therefore, a plane-wave approximation for the pump beam, whether continuous wave or pulsed, is valid for the experimental results presented in this work, and indeed for most quantum-interference experiments.

[1] S.E. Harris, M.K. Oshman, and R.L. Byer, Phys. Rev. Lett. **18**, 732 (1967); D. Magde and H. Mahr, *ibid.* **18**, 905 (1967).

[2] E. Schrödinger, Naturwissenschaften **23**, 807 (1935); **23**, 823 (1935); **23**, 844 (1935); [Translation: J.D. Trimmer, Proc. Am. Philos. Soc. **124**, 323 (1980); reprinted in *Quantum Theory and Measurement*, edited by J. A. Wheeler and W. H. Zurek (Princeton University Press, Princeton, 1983)].

[3] C.K. Hong, Z.Y. Ou, and L. Mandel, Phys. Rev. Lett. **59**, 2044 (1987); P.G. Kwiat, A.M. Steinberg, and R.Y. Chiao, Phys. Rev. A **47**, R2472 (1993).

[4] J.G. Rarity and P.R. Tapster, Phys. Rev. Lett. **64**, 2495 (1990).

[5] Z.Y. Ou and L. Mandel, Phys. Rev. Lett. **61**, 50 (1988); Y.H. Shih and C.O. Alley, *ibid.* **61**, 2921 (1988); Y.H. Shih and A.V. Sergienko, Phys. Lett. A **191**, 201 (1994); P.G. Kwiat, K. Mattle, H. Weinfurter, A. Zeilinger, A.V. Sergienko, and Y.H. Shih, Phys. Rev. Lett. **75**, 4337 (1995).

[6] A. Joobeur, B.E.A. Saleh, and M.C. Teich, Phys. Rev. A **50**, 3349 (1994); C.H. Monken, P.H. Souto Ribeiro, and S. Pádua, *ibid.* **57**, 3123 (1998); B.E.A. Saleh, A. Joobeur, and M.C. Teich, *ibid.* **57**, 3991 (1998).

[7] B.E.A. Saleh, A.F. Abouraddy, A.V. Sergienko, and M.C. Teich, Phys. Rev. A **62**, 043816 (2000).

[8] D. N. Klyshko, *Photons and Nonlinear Optics* (Gordon and Breach, New York, 1988).

[9] T.B. Pittman, D.V. Strekalov, D.N. Klyshko, M.H. Rubin, A.V. Sergienko, and Y.H. Shih, Phys. Rev. A **53**, 2804 (1996).

[10] B.R. Mollow, Phys. Rev. A **8**, 2684 (1973); M.H. Rubin, *ibid.* **54**, 5349 (1996).

[11] M. Atatüre, G. Di Giuseppe, M.D. Shaw, A.V. Sergienko, B.E.A. Saleh, and M.C. Teich, Phys. Rev. A **65**, 023808 (2002).

[12] M. Atatüre, A.V. Sergienko, B.M. Jost, B.E.A. Saleh, and M.C. Teich, Phys. Rev. Lett. **83**, 1323 (1999).

[13] G. Di Giuseppe, L. Haiberger, F. De Martini, and A.V. Sergienko, Phys. Rev. A **56**, R21 (1997); T.E. Keller and M.H. Rubin, *ibid.* **56**, 1534 (1997); W.P. Grice, R. Erdmann, I.A. Walmsley, and D. Branning, *ibid.* **57**, R2289 (1998).

[14] J. Peřina, Jr., A.V. Sergienko, B.M. Jost, B.E.A. Saleh, and M.C. Teich, Phys. Rev. A **59**, 2359 (1999).

[15] P.G. Kwiat, E. Waks, A.G. White, I. Appelbaum, and P.H. Eberhard, Phys. Rev. A **60**, R773 (1999); S. Tanzilli, H. De Riedmatten, W. Tittel, H. Zbinden, P. Baldi, M. De Micheli, D.B. Ostrowsky, and N. Gisin, Electron. Lett. **37**, 26 (2001); C. Kurtsiefer, M. Oberparleiter, and H. Weinfurter, e-print quant-ph/0101074.

[16] For a review of spectral tuning through angular dispersive elements, see, for example, J. -C. Diels and W. Rudolph, *Ultrashort Laser Pulse Phenomena* (Academic Press, San Diego, 1996), Chap. 2.

[17] Y.H. Kim, V. Berardi, M.V. Chekhova, and Y.H. Shih, Phys. Rev. A **64**, 011801(R) (2001).

[18] G. Di Giuseppe, M. Atatüre, M. D. Shaw, A. V. Sergienko, B. E. A. Saleh, and M. C. Teich, Phys. Rev. A **66**, 013801 (2002).

[19] M. Born and E. Wolf, *Principles of Optics*, 7th ed. (Cambridge University Press, Cambridge, 1999).

[20] D.N. Klyshko, Sov. Phys. JETP **56**, 753 (1982); *Photons and Nonlinear Optics* (Ref. [8]), Chap. 6.3.